CARBON 50 (2012) 3561–3571

Available at www.sciencedirect.com

SciVerse ScienceDirect

journal homepage: www.elsevier.com/locate/carbon

The effect of temperature on the mechanism of photoluminescence from plasma-nucleated, nitrogenated carbon nanotips

B.B. Wang [a,b], Q.J. Cheng [b,c], L.H. Wang [d], K. Zheng [d], K. Ostrikov [b,c,*]

[a] College of Chemistry and Chemical Engineering, Chongqing University of Technology, 69 Hongguang Rd., Lijiatuo, Banan District, Chongqing 400054, PR China

[b] Plasma Nanoscience Centre Australia (PNCA), CSIRO Materials Science and Engineering, P.O. Box 218, Lindfield, NSW 2070, Australia

[c] Plasma Nanoscience, School of Physics, The University of Sydney, Sydney, NSW 2006, Australia

[d] Institute of Microstructure and Properties of Advanced Materials, Beijing University of Technology, Beijing 100124, PR China

ARTICLE INFO

Article history:
Received 30 November 2011
Accepted 13 March 2012
Available online 21 March 2012

ABSTRACT

Nitrogenated carbon nanotips (NCNTPs) have been synthesized using customized plasma-enhanced hot filament chemical vapor deposition. The morphological, structural, and photoluminescent properties of the NCNTPs are investigated using scanning and transmission electron microscopy, X-ray photoelectron spectroscopy, Raman spectroscopy, and photoluminescence spectroscopy. The photoluminescence measurements show that the NCNTPs predominantly emit a green band at room temperature while strong blue emission is generated at 77 K. It is shown that these very different emission behaviors are related to the change of the optical band-gap and the concentration of the paramagnetic defects of the carbon nanotips. The studies shed light on the controversies on the photoluminescence mechanisms of carbon-based amorphous films measured at different temperatures. The relevance of the results to the use of nitrogenated carbon nanotips in light-emitting optoelectronic devices is discussed.

1. Introduction

Recently, low-dimensional nanomaterials have received considerable attention due to their tremendous contributions to fundamental science and industrial applications [1–4]. In particular, carbon-related nanomaterials with a huge variety of structures in all three dimensions, such as C_{60}, single and multi-walled nanotubes, nanorods, nanofibers, graphenes, nanofilms, nanoribbons, nanocones, nanotips, and several others, have been in the spotlight of extensive research efforts owing to their novel structures and outstanding chemical and physical properties [5–11]. Among these carbon nanomaterials, carbon nanotips (CNTPs) can be prepared at low temperatures and pressures, and they can form crystalline and amorphous phases with controllable degrees of crystallinity and tunable concentration of sp^2 bonding configuration [11,12]. Moreover, the nanotips feature high aspect ratios and weak electric field screening effects due to their sharp tip structure. Interesting structural and electronic properties of CNTPs make them promising for numerous applications in the field of microelectronic and optoelectronic technology, with relevant applications including scanning microscope probes, electron field emitters, and several others [13,14].

Traditionally, the CNTPs and related materials such as carbon nanotubes and carbon nanocones have been targeted for

* *Corresponding author at:* Plasma Nanoscience Centre Australia (PNCA), CSIRO Materials Science and Engineering, P.O. Box 218, Lindfield, NSW 2070, Australia. Fax: +61 02 9413 7200.
E-mail address: kostya.ostrikov@csiro.au (K. Ostrikov).

0008-6223/$ - see front matter
http://dx.doi.org/10.1016/j.carbon.2012.03.028

field emission devices. Recently, the range of applications of such nanocarbons has been extended to biological and medical uses due to their biocompatibility. For instance, carbon nanotubes can be used for biological imaging and drug delivery [15].

Another promising application of the CNTPs is in the area of light emitting and other optoelectronic devices. This is because carbon-based amorphous films, e.g., *a*-C:H and *a*-C:N:H films, have been reported as good light emitting sources [16–21]. However, the physical mechanisms of photoluminescence (PL) emission from carbon-based amorphous films measured at different temperatures are not clearly understood. For example, the results of Chernyshov et al. [17] indicate that the PL from *a*-C:H films shows a poor temperature dependence, while the results of Liao et al. [18] show that the PL from a-C:H films has a complex, non-monotonic (i.e., the PL intensity initially decreased, and then increased significantly with the increase of the temperature) dependence on temperature. Furthermore, Papadimitriou et al. [21] observed that the PL intensity from *a*-C:N films measured at 20 K increased by two orders of magnitude compared to the PL intensity measured at 300 K.

Although it is commonly accepted that the PL emission from amorphous carbon films originates from the radiative recombination of electrons and holes in the band tail states of sp^2 carbon clusters [16], there is no consensus on the dominant mechanisms of photoluminescence at different temperatures. For example, Liao et al. [18] suggested that the temperature-dependence of PL was related to the change in the structure of the films. Papadimitriou et al. [21] attributed the increase of PL intensity to an increase of defect concentration through the creation of dangling bonds in the films at low temperatures. Robertson [16] argued that the PL efficiency depended on the defect concentration in the absence of hopping at high temperatures. On the other hand, Ilie et al. [22] claimed that the non-radiative recombination through defects was significantly suppressed because, at low temperatures, the mobility of carriers is very low and their transport may only occur by energy-loss hopping in the band tails. In this case, the carriers thermalize deeper into the tail states than into deep defect states.

Very recently, it was found that the carbon nanotip structures with a modest hydrogen and nitrogen incorporation can generate photoluminescence [23]. For these doped CNTPs, there is much less understanding of the PL mechanism due to the very limited number of reports available. Inspired by many successful works on the unique structural and electronic properties of the CNTPs compared with carbon-based amorphous films, here we study the properties and mechanisms of PL from nitrogenated CNTPs (NCNTPs) at room and low temperatures. It is revealed that the NCNTPs predominantly emit a green band at room temperature, whilst strong blue emission is generated at low temperatures. By investigating the morphological, structural, and PL properties of the NCNTPs, as well as examining PL mechanisms of carbon-based amorphous films, we propose viable physical mechanisms of the NCNTP photoluminescence to interpret the experimental results.

2. Experimental

Nitrogenated carbon nanotips have been synthesized in a two-step process. In the first step, a thin carbon film with a thickness of about 60 nm has been deposited onto a Si(100) substrate using a rf magnetron sputtering deposition system. This thin carbon film acts as a seed layer for the subsequent nucleation and growth of NCNTPs [11].

During the second step, the NCNTPs were synthesized in a custom-designed plasma-enhanced hot filament chemical vapor deposition (PEHFCVD) system. The details of the plasma reactor and its operation can be found elsewhere [11]. Briefly, a mixture of CH_4, N_2 and H_2 precursor gases was let into the chamber which had been pre-evacuated to a base pressure of approximately 2 Pa through the use of a two-stage rotary pump. The total working gas pressure was maintained at 2×10^3 Pa. The filament was then rapidly heated to about 1600 °C with the substrate surface temperature estimated to be approximately 800 °C (measured using a thermocouple). Later, a bias with a preset DC current was applied to produce plasmas and deposit NCNTPs. The detailed experimental parameters for the growth of NCNTPs are listed in Table 1. It is noteworthy that a minor variation of the measured bias voltage at the same applied bias current is due to the change of the N_2 and H_2 mass flow rates.

The morphological, structural, and photoluminescence properties of the synthesized samples were characterized using various advanced analytical tools, including scanning electron microscopy (SEM), X-ray photoelectron spectroscopy (XPS), high-resolution transmission electron microscopy (HRTEM), Raman spectroscopy, and PL spectroscopy. SEM measurements were conducted using a Hitachi-S4800 field emission scanning electron microscope operated at 15 kV. HRTEM measurements were carried out using a JEOL 2010F (operated at 200 kV) transmission electron microscope. Raman measurements were performed using a Renishaw *in*Via micro-Raman system with a 514.5 nm Ar^+ laser as an excitation source. The temperature-dependent PL measurements were undertaken via a SPEX 1403 Ramalog system using a 325 nm He–Cd laser as an excitation source. In order to investigate the effect of the excitation energy on the PL property of NCNTPs, a HR 800 micro-Raman system using a semiconductor laser at 532 nm line as an excitation source has also been used to perform the PL measurements. The XPS measurements were carried out via an ESCALAB 250 X-ray photoelectron spectrometer using a Al *K*α X-ray source.

3. Results

Fig. 1(a) and (b) show the SEM image and the Raman spectrum of the thin carbon seed layer, respectively. From Fig. 1(a), one can clearly see that the thickness of the carbon film is approximately 60 nm and that the interface between the Si substrate and the film layer is well resolved and clear of defects. Two scattering peaks centered about 1394 and 1578 cm^{-1}, shown in Fig. 1(b), are attributed to the D and G peaks of the carbon material [17,18]. The intensity ratio of the D to G peak is about 0.66, which suggests that the carbon film is amorphous [19].

Table 1 – Deposition parameters for the samples A and B: mass flow rates of CH_4, H_2 and N_2 gases; substrate temperature T_s; bias current I_b and voltage U_b; growth time t.

Sample	CH_4 (sccm)	H_2 (sccm)	N_2 (sccm)	T_s (°C)	I_b (mA)	U_b (V)	t (min)
A	20	70	10	792	160	980	16
B	20	65	15	796	160	930	20

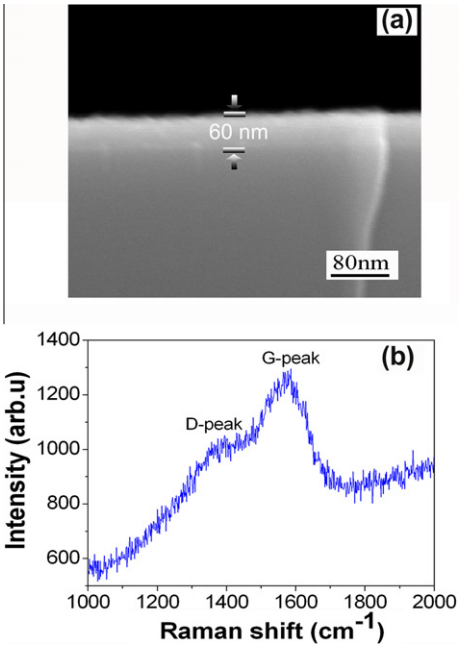

Fig. 1 – SEM image (a) and Raman spectrum (b) of the thin carbon seed layer.

Fig. 2(a) presents the typical cross-sectional SEM image of sample A. One can notice that the NCNTPs feature a needle-like shape. The typical bottom width, top diameter, and height of the NCNTPs estimated from the SEM images are within the ranges 58–92, 25–42, and 292–417 nm, respectively. Fig. 2(b) shows a typical cross-sectional TEM image of the individual NCNTPs. The layered structure (Si/*a*-C/NCNTPs) can be clearly viewed from the image and the interface between *a*-C and NCNTPs is very sharp. The TEM result is consistent with the SEM analysis. HRTEM imaging (Fig. 2(c)) shows that the synthesized NCNTPs are amorphous.

Fig. 3(a) and (b) show typical low- and high- magnification SEM images of sample B. One can notice that the morphology of this sample is quite similar to that of sample A. However, the bottom width, top diameter, and height of the NCNTPs are different from those of sample A. In this case, the bottom width, top diameter, and height of the NCNTPs are within the ranges 50–75, 13–17, and 158–375 nm, respectively.

Fig. 3(c) shows the Raman spectrum of sample B. Two broad Raman scattering peaks located at about 1350 and1609 cm^{-1} can be observed, which can be assigned to the D and G peaks of amorphous carbon materials [8,24]. In comparison with the Raman spectrum for the thin carbon film seed layer (shown in Fig. 1(b)), the G peak shows a blue-shift of about 31 cm^{-1}, which suggests that nitrogen atoms

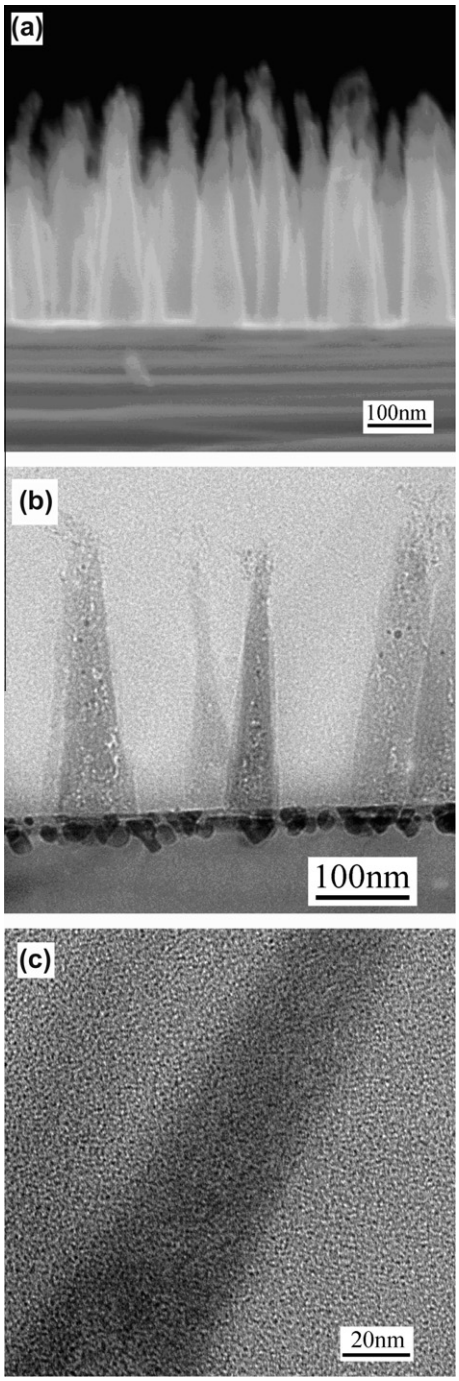

Fig. 2 – SEM and TEM images of the sample A: (a) cross-sectional SEM image; (b) cross-sectional TEM image; (c) high-resolution TEM image.

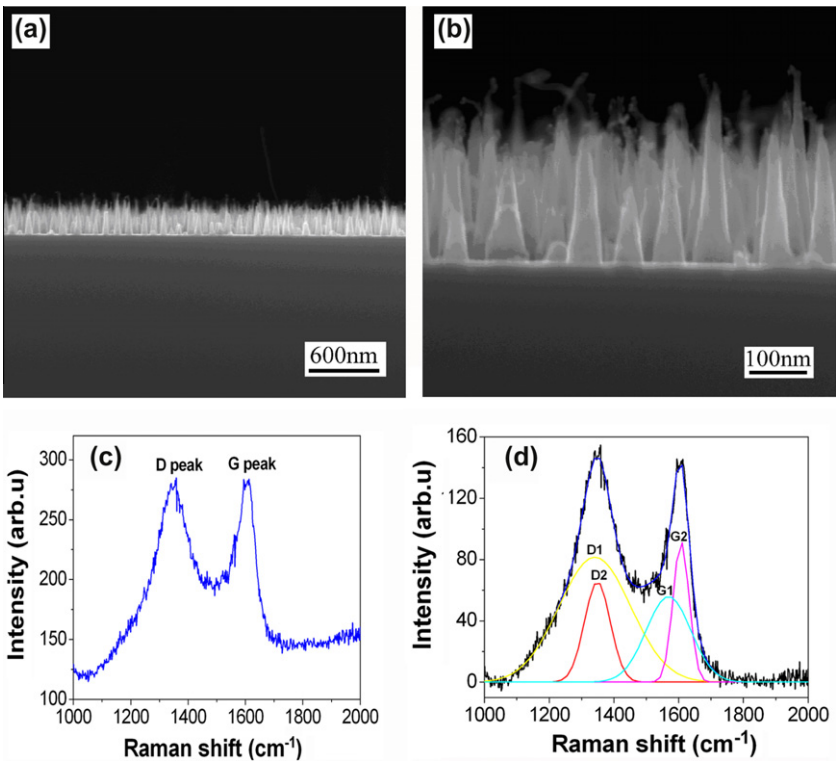

Fig. 3 – SEM images and Raman spectrum of the sample B: (a) low-magnification SEM image; (b) high-magnification SEM image; (c) Raman spectrum; (d) deconvoluted Raman spectrum. Positions of D1, D2, G1, and G2 peaks are given in Table 2.

have been effectively incorporated into the carbon nanotips [25].

The asymmetry of Raman bands implies that they are composed of many different peaks. Therefore, this spectrum can be fit and deconvoluted following the approach proposed by Kovács et al. [26]. The deconvoluted Raman spectrum is presented in Fig. 3(d). One can notice that the spectrum consists of four Gaussian components: D1, D2, G1, and G2. The details of these Gaussian peaks including the peak position, full width at half maximum (FWHM), intensity, etc., are shown in Table 2. Since the peak position of G1 (1568 cm^{-1}) is lower than 1580 cm^{-1} (standard G peak of graphite) while the peak position of G2 (1610 cm^{-1}) is higher than 1580 cm^{-1}, we can deduce that the D1-G1 and D2-G2 pairs belong to the clusters composed of sp^2 carbon atoms in chains and rings, respectively [26].

Fig. 4(a) displays a typical wide-scan XPS spectrum of sample B. The dominant peaks are located at binding energies (BEs) of about 284.6, 399.6, and 531.96 eV, which stem from carbon, nitrogen and oxygen elements, respectively. To investigate the bonding states of the synthesized NCNTPs in detail, narrow-scan XPS spectra of C 1s, N 1s and O 1s states were measured. Fig. 4(b)–(d) present the narrow scan XPS spectra of the C 1s, N 1s, and O 1s states, respectively. The broadness and asymmetry of the C 1s, N 1s and O 1s XPS spectra suggest that multi-component peaks should exist. This is why we have used Casa XPS peak software to fit these spectra using a least-square routine, after Shirley background subtraction. The detailed deconvoluted peaks (including peak position and FWHM) for the individual C1s, N 1s, and O 1s spectra are shown in Table 3. Amongst these peaks, the A–C peaks in Fig. 4(b) are attributed to sp^2 C–C, sp^3 C–C, and sp^3 C–N bonds, respectively [27–29]; the D and E peaks in Fig. 4(c) originate from sp^3 and sp^2 C–N bonds, respectively [29]; and the F and G peaks in Fig. 4(d) can be assigned to the —OH and —C=O groups on the surface of NCNTPs, respectively [30].

Fig. 5(a) shows the PL spectra of sample B measured at 77 K (1) and 300 K (2), respectively. One can see that both PL spectra are composed of two emission bands. At 300 K, these two emission bands are centered at ~406 and ~508 nm, while at

Table 2 – Peak positions, full widths at half maximum (FWHMs), and intensities of D1, D2, G1, G2 Gaussian components for the sample B.

Peak	Ramanshift (cm^{-1})	FWHM (cm^{-1})	Intensity
D1	1341	221	22653
D2	1349	80	6591
G1	1568	138	9664
G2	1610	50	5725

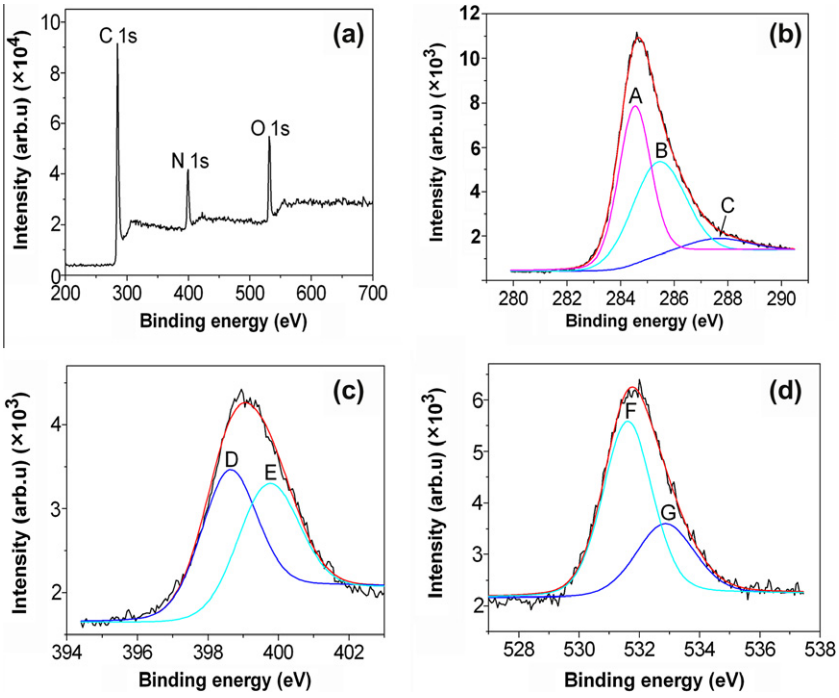

Fig. 4 – XPS spectra for the sample B: (a) wide-scan XPS spectrum; (b)–(d) narrow scan XPS spectra of the C 1s (b), N 1s (c), and O 1s (d). Positions of deconvoluted peaks A, B, C, D, E, F, and G can be found in Table 3.

Table 3 – Peak positions and FWHMs of the deconvoluted peaks for the individual C1s, N 1s, and O 1s spectra for the sample B.

Peak	A	B	C	D	E	F	G
BE (eV)	284.6	285.5	287.7	398.7	399.8	531.6	532.9
FWHM (eV)	1.24	2.05	2.98	1.65	1.8	1.66	1.95

77 K the same bands are located at approximately 403 and 502 nm. It is obvious that the PL bands show a slight blue-shift when the measurement temperature is reduced from 300 to 77 K. More importantly, one can notice that the dominant emission peak changes from 508 nm (green peak) at 300 K to 403 nm (blue peak) at 77 K.

Fig. 5(b) shows the room-temperature PL spectrum of sample B recorded by a HR 800 micro-Raman spectroscope using a semiconductor laser at 532 nm line as the excitation source. One can notice that five peaks are present in the spectrum. Two sharp peaks located at 573 and 582 nm originate from Raman scattering of NCNTPs. This can be explained as follows. According to the definition of the Raman shift (RS), the relationship of the RS with the scattering wavelength λ_S is

$$RS = \frac{1}{\lambda_L} - \frac{1}{\lambda_S} \quad (1)$$

where λ_L is the wavelength of the excitation source [31]. Following this formula, the calculated values for the RS corresponding to the observable sharp peaks at 573 and 582 nm are approximately 1345 and 1614 cm^{-1}, which are in good agreement with the corresponding Raman scattering peaks observed in Fig. 3(c). The other three weak peaks located at 620, 630, and 686 nm can be attributed to the photo-induced emission of NCNTPs.

4. Discussion

As shown in Fig. 5(a), the NCNTPs emit two PL bands. Moreover, the emission behavior of the NCNTPs at room and low temperatures is different. In this section, a detailed physical mechanism is proposed to explain this phenomenon. We believe that the different emission behaviors at room and low temperatures are related to the significant structural changes and the corresponding variation of electronic properties of NCNTPs.

4.1. *Purpose of nitrogen addition*

In our experiments, we found that no carbon nanotips could be produced in our CVD system using only methane and hydrogen as reactive gases. After the detailed analysis of the formation process of the carbon nanotips, we believe that this failure possibly involves the interaction of oxygen with the substrate and a weak bombardment of hydrogen ions produced in the plasma. To be more specific, during the process

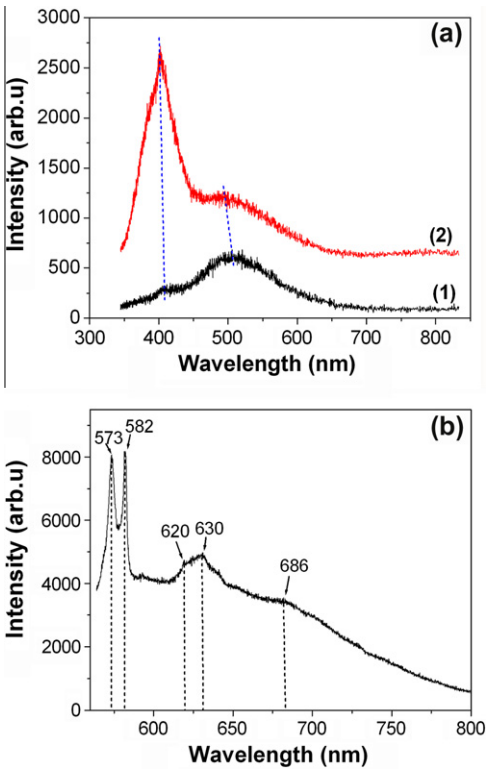

Fig. 5 – PL spectra of the sample B: (a) measured using 325 nm line at different temperatures: (1): 300 K and (2): 77 K; (b) measured using 532 nm line at room temperature.

of substrate heating, the interaction between the residual oxygen molecules and the substrate is unavoidable, which prevents the nucleation and growth of carbon nanotips.

By adding nitrogen gas to the methane and hydrogen reactive mixture, oxygen atoms can be removed from the substrate fairly quickly because of the strong electronegativity and the large mass of nitrogen compared with hydrogen. Moreover, interaction of nitrogen ions with the surface can accelerate the nucleation of carbon radicals and the subsequent formation of carbon nanotips [11]. More importantly, nitrogen incorporation in the amorphous carbon films is able to promote the transformation of sp^3 carbon to sp^2 carbon, leading to the significant increase of the total number of sp^2 clusters [32]. In addition, some energetic nitrogen ions can effectively bombard sp^2 carbon clusters and drastically reduce their size. With the addition of nitrogen gas, the variation in the number and size of sp^2 clusters and the accompanied incorporation of nitrogen in the clusters can alter the PL properties of carbon materials quite significantly.

4.2. *Effect of experimental parameters on the morphological, structural, and PL properties of NCNTPs*

Our previous experimental works show that, the NCNTPs deposited at an intermediate flow rate ratio of hydrogen to nitrogen of approximately 4 (for example, sample B in this work) feature the best size/shape and pattern uniformity, as well as the highest nanotip density, compared with other NCNTPs synthesized at higher or lower flow rate ratios of hydrogen to nitrogen [33]. This can be interpreted in terms of the combined effect of the sputtering and etching of NCNTPs by nitrogen-based ions/radicals and hydrogen atoms during the growth process.

In a typical plasma-based growth process of NCNTPS, nitrogen-based ions including N_2^+, NH_2^+, NH_3^+ and NH_4^+, etc., are generated in the plasma and these ions make a significant contribution to the sputtering and etching of the surface of NCNTPs [33,34]. At a high flow rate ratio of hydrogen to nitrogen (e.g., sample A used in this work), the number of nitrogen-based radicals is rather limited so that the sputtering effect is fairly weak. As a result, the deposition rate of carbon increases, eventually resulting in a poor uniformity of NCNTPs. In addition, hydrogen etching of amorphous carbon further deteriorates the uniformity of the NCNTPs.

If the flow rate ratio of hydrogen to nitrogen is too low, the number of nitrogen-based ions with a large mass increases significantly [33,34]. In this case, the sputtering effect during the growth of NCNTPs is very strong. At the same time, the etching rate of the nanostructured carbon surface becomes higher due to the higher nitrogen flow rate. The reason is that the etching rate is proportional to the product of the flux of reactive ions and the reaction probability [33,34]. As a consequence, the strong sputtering and etching effects at a low flow rate ratio of hydrogen to nitrogen also lead to a low density and poor uniformity of NCNTPs.

The flow rate ratio of hydrogen to nitrogen can be optimized to reduce the effects of the sputtering and etching of the growth surfaces of NCNTPs by nitrogen-based ions and hydrogen atoms. In this case, the sputtering/etching and deposition processes are in a dynamical balance, and the uniform NCNTP structures can be formed [11].

However, the structural and photoluminescence properties of NCNTPS do not change significantly under different flow rate ratios of hydrogen to nitrogen. HRTEM measurements show that all the NCNTPs are amorphous; Raman and PL measurements reveal that all the NCNTPs have quite similar peak positions and intensities. That is why the Raman, HRTEM, and PL results collected from samples A or B are only shown here.

4.3. *Structural and electronic properties of NCNTPs at low temperatures*

Figs. 3 and 4 indicate the presence of sp^2 C–C, sp^2 C–N, sp^3 C–C, and sp^3 C—N bonds in the NCNTP structures. Importantly, the lengths of these bonds change with temperature. Mandal et al. [35] reported that the mean distances between the two nearest neighbor carbon atoms in the molecule composed of phenalenyl units were 3.26 and 3.30 Å at 100 and 300 K, respectively. The corresponding distances for the molecule composed of ethyl radicals were 3.18 and 3.35 Å at 100 and 293 K, respectively. These results suggest that the bond lengths for sp^2- and sp^3-hybridized configurations become shorter at low temperatures. As a result, the size of sp^2 and sp^3 carbon clusters reduces so that the band-gap of the NCNTPs increases [36,37]. The variation of the band-gap with temperature has also been observed in the synthesized diamond-like materials [38].

At low temperatures, another important property of carbon-based materials, namely, paramagnetic defects, can change significantly. For example, Watanabe et al. [39] reported that the electron spin resonance signal in the amorphous carbon films could be observed at low temperatures after UV illumination. This is because there are very few paramagnetic defects in the amorphous carbon films at low temperatures, and some C—H and C—C bonds can be broken during sufficiently long UV irradiation [39,40]. The significant reduction of paramagnetic defects at low temperatures is likely due to the re-arrangement of carbon atoms caused by the increased bond energies which are a consequence of the shortened bond lengths. The increase of the band-gap and the reduction of paramagnetic defects are two significant factors that affect the photoluminescence efficiency of amorphous carbon films [16]. This effect will be discussed in the following sub-section.

4.4. Photoluminescence of NCNTPs at low temperatures

4.4.1. Analysis of the blue shift of PL bands at low temperatures

For the amorphous carbon films, it is generally accepted that the PL emission originates from the radiative recombination of the electrons and holes in the band tail of sp^2 carbon clusters, which are created by photo-excitation in π and π^* states [16]. Thus, the PL process is closely related to the π and π^* states. As follows from Fig. 4(c), sp^2 and sp^3 C—N bonds are formed in the NCNTPs. This in turn suggests that nitrogen atoms have effectively substituted carbon atoms in these sp^2 and sp^3 C—C clusters. As a result, the lone pair (LP) electrons in the sp^2 and sp^3 C—N bonds can form LP states within the π band and between the π and π^* bands, respectively [36,37,41,42].

However, Füle et al. [43] reported that, in order to enable the direct transition between the π and π^* bands, the size of sp^2 carbon clusters should be within the range 0.94–1.15 nm. For the NCNTPs considered here, the size of the sp^2 clusters L can be estimated by

$$\frac{I_D}{I_G} = \frac{-126 + 0.033\lambda}{L} \quad (2)$$

where I_D and I_G are the integrated intensities of the D and G Raman peaks, and λ is the laser excitation wavelength [21]. Using the data shown in Table 2, the calculated size of the sp^2 clusters in chains and rings appears to be about 1.9 and 3.8 nm, respectively. Thus, it is unlikely that the direct transition between the π and π^* bands is generated in our samples. Therefore, we conclude that the PL bands centered about 406 and 508 nm are attributed to the transition between the σ^* and LP valence bands which are related to sp^2 and sp^3 C—N bonds, respectively [23].

As mentioned previously, at low temperatures, the shortening of the bond lengths results in the size reduction of the sp^2 carbon clusters so that the band-gap is increased [36,37]. Therefore, the separation between the π and π^* bands also increases [44,45]. At the same time, the LP valence band shifts in the direction of the π band [41], which is indicative of the increase in the separation between the LP valence and π^* bands at low temperatures. For example, Heitz et al. [44,45] reported that the PL peak shifted from 2.4 to 2.2 eV when E_{04} (i.e., the energy of the photons for which the absorption coefficient is 10^4 cm^{-1}) decreased from 4.0 to 1.5 eV, and that the separation between the π and π^* bands became larger with the increase of E_{04}. Therefore, the separation between the π and π^* bands may become comparable or even larger than the PL peak energies. Moreover, due to the size reduction of sp^2 carbon clusters, it is likely that there are more sp^2 carbon clusters of about 1 nm at low temperatures. Hence, the probability of the direct transition between the π and π^* bands also becomes higher. Furthermore, at low temperatures, the recombination of electrons and holes is dominated by the radiative recombination in the band tail of sp^2 carbon clusters [22].

According to the above analyses and the PL mechanism suggested by Iwano et al. [20], the PL band at 502 nm may be assigned to the transition between the π^* and LP valence bands, which is related to sp^3 C—N bonds. On the other hand, the PL band at 403 nm may be assigned to the transition between the π^* and LP valence bands and between the π and π^* bands, which is related to sp^2 C—N bonds. Moreover, due to the increase in the separation between the π and π^* bands at low temperatures, the PL spectra are slightly blue-shifted compared to the spectra at room temperature.

4.4.2. Interpretation of generation of strong blue emission band at low temperatures

As shown in Fig. 5, a strong blue emission band located at about 400 nm has been observed at low temperatures. The origin of the blue emission peak at low temperatures is possibly due to the combined effect of the increase in band-gap and band tail width, the reduction of paramagnetic defects, and weaker thermal vibration of atoms. These effects enhance the efficiency of photoluminescence generated by amorphous carbon materials.

It has been shown previously that the PL efficiency of amorphous carbon films increases in an exponential fashion with the increase of the optical band-gap [16]. Thus, the PL efficiency of the NCNTPs is significantly enhanced at low temperatures due to the significant increase of the band-gap (see the detailed analysis in Section 4.4.1).

At low temperatures, the reduction in the size of sp^2 clusters can also lead to the higher degree of localization so that the width of the band tail distribution is increased [22,43]. It is generally believed that the relation of the PL quenching temperature T_L with the width E_0 of the band tail distribution is expressed as follows,

$$k_B T_L = E_0 / \ln(\nu_0 \tau_0) \quad (3)$$

where k_B is the Boltzman constant, ν_0 is the hopping attempt frequency (typically 10^{12}–10^{13} s^{-1}), and $\tau_0 = 10^{-8}$ s [16,22]. From this equation, one can clearly see that T_L is directly proportional to E_0. Furthermore, the relationship between the PL efficiency and the temperature is expressed by

$$\eta \propto \exp\left(-\frac{T}{T_L}\right) \quad (4)$$

where T and η are the temperature and the PL efficiency, respectively [16]. From Eq. (4), it is obvious that the PL efficiency increases exponentially with the decrease of the temperature due to the significant increase of T_L.

As mentioned in Section 4.3, the paramagnetic defects are greatly reduced in amorphous carbon films at low temperatures. This makes the radiative recombination of electrons and holes as the dominant recombination process in this case. It was previously reported that non-radiative recombination in amorphous carbon nitride films becomes less important at low temperatures [22]. Therefore, it is likely that the PL efficiency increases through the reduction of paramagnetic defects.

At low temperatures, the recombination of electrons and holes is dominated by the radiative recombination in the band tail of sp^2 carbon clusters [22]. In this case, the PL emission is generated by the transition between the π^* and π bands. In addition, the thermal vibration of atoms is weakened at low temperatures. Hence, the effect of scattering of incident photons by phonon vibrations becomes weaker thereby increasing their energy. In this way, the enhancement factors mentioned above may lead to the substantial increase of the PL efficiency of the emission band at 403 nm. As a result, a strong blue emission band can be observed at low temperatures.

4.5. *Explanation of PL of a-C:H and a-C:N films at different temperatures*

The analysis in Section 4.4 indicates that the PL of amorphous carbon materials can be effectively controlled by the size of sp^2 clusters and the paramagnetic defects. Clear understanding of these effects may resolve several persistent controversies on the origin of photoluminescence from *a*-C:H and *a*-C:N films at different temperatures.

It was previously reported that the dependence of the PL on temperature was quite weak [17]. This result may be due to the insufficient energy of the photons from the excitation source, which was not specified in Ref. [17]. Indeed, PL can only be emitted when the excitation energy is larger than the band-gap energy or the transition energy. When the measurement temperature decreases, the sp^2 clusters become smaller and their band-gaps increase. In this case, the excitation with a short wavelength should be used; otherwise some of the sp^2 clusters may not produce photoemission. This is why the weak temperature dependence of PL of *a*-C:H films is most likely a measurement-specific, rather than a common observation.

Furthermore, the results of Liao et al. [18] showed that PL from *a*-C:H films had a complex dependence on temperature. Specifically, the PL intensity initially decreased with temperature between 25 and 75 K, and then increased, eventually reaching its maximum value at 250 K. Since the sizes of sp^2 clusters in *a*-C:H films vary quite significantly, the band-gap distribution is also quite non-uniform. The band-gaps of small clusters are large and higher-energy photons are needed to generate the emission. When the measurement temperature decreases, their band-gaps will further increase. As a result, the PL from some sp^2 clusters may no longer be generated using the same excitation source. Therefore, the PL intensity is reduced at lower temperatures. After the temperature is reduced below a certain threshold, the band-gaps of some relatively large sp^2 clusters increase and they may start emitting PL. However, the number of these clusters is quite small, which leads to weaker PL at low temperatures. On the other hand, at high temperatures the rates of non-radiative recombination via defects increase, which explains the observed weaker photoluminescence at higher temperatures. The interplay of these effects explains the observed non-monotonic temperature-dependent PL from *a*-C:H films [18].

For the *a*-C:N films, Papadimitriou et al. [21] observed that the PL intensity measured at 20 K increased by two orders of magnitude compared with the results at 300 K. They attributed this significant intensity increase to the creation of a large number of defects (mainly dangling bonds) at low temperatures. However, the dangling bonds are believed to be the non-radiative recombination centers, which contribute to the quenching of the emission [46]. Therefore, the increase of the PL intensity at low temperatures may be attributed to the effects of weaker thermal vibration of atoms and the increase of the band-gap at low temperatures, according to the analysis presented in Section 4.4.

We emphasize that in this work we were only able to measure PL at 77 K and room temperature by using a 325 nm laser. However, the following effects are expected with the gradual decrease of measurement temperatures from 300 to 77 K:

(i) The green peak located at 508 nm measured at 300 K should show a slight blue-shift and eventually reach the 502 nm position measured at 77 K. Moreover, the intensity of this peak is expected to show a tendency to decrease.
(ii) The blue peak located at 406 nm measured at 300 K should also display a tendency of up-shift and eventually reach the 403 nm position measured at 77 K. Moreover, the intensity of this peak should show a trend of gradual increase.

These expectations are based on the combined effect of the variation of optical band-gap, band tail width, paramagnetic defects, and thermal vibration of atoms as we have discussed previously. To be more specific, with the increase of the PL measurement temperature, the band-gap and band tail width decrease. This is caused by the longer bond lengths for sp^2- and sp^3-hybridized configurations at a higher measurement temperature. This gives rise to the red-shift of PL peaks of both 403 and 502 nm with the increase of the measurement temperature. It also explains the gradually increased PL peak intensity of 502 nm and the gradually decreased PL intensity of 403 nm. Indeed, at a higher measurement temperature, the total number of clusters with smaller band-gaps increases significantly, which leads to the increased PL peak intensity of 502 nm and the decreased PL peak intensity of 403 nm. Furthermore, the increased paramagnetic defects (main non-radiative recombination centers) and strong thermal vibration of atoms at a higher measurement temperature further reduce the intensity of the 403 nm peak. This is because in this case the photo-generated carriers produced across the band-gaps have a high chance of non-radiative recombination through hopping or tunneling, and do not contribute to the PL emission [47].

In comparison with the previous works, we have accounted for many factors such as the optical band-gap, band tail width, paramagnetic defects, and thermal vibration of atoms. Careful consideration of these effects leads to better understanding of the mechanisms of temperature-dependent PL emission. We have also considered the variation of size of sp^2 and sp^3 carbon clusters at different temperatures and their effects on the PL process. Moreover, the PL bands centered about 406 and 508 nm have been attributed to the transition between the σ^* and LP valence bands which are related to sp^2 and sp^3 C–N bonds, respectively.

4.6. Analysis of PL bands under the 532 nm excitation

As shown in Fig. 5(b), three PL bands located at 620, 630 and 686 nm are generated under the 532 nm laser excitation. For the PL bands at 620 and 630 nm, their generation is related to the large sp^2 clusters. This follows from the following analysis. As presented previously in Section 4.4, the PL generation results from the transition between the two bands. From Fig. 3(b), one can see that the size distribution of the NCNTPs is broader. In addition, the wide D and G peaks shown in Fig. 3(c) imply that the size distribution of the particles also becomes broader. For the large sp^2 clusters, their band-gaps become narrower so that the separation between the two bands reduces. Namely, the separations between the π^* and LP valence bands and between the π and π^* bands become smaller. That is why the 620 and 630 nm PL peaks can be observed under the 532 nm laser excitation. To be more specific, the PL band at 630 nm results from the transition between the π^* and LP valence bands, which is related to sp^3 C—N bonds. On the other hand, the PL band at 620 nm originates from the transition between the π^* and LP valence bands and between the π and π^* bands, which is related to sp^2 C—N bonds. The PL band at 686 nm presumably originates from the —OH radicals on the surfaces of NCNTPs. A similar PL peak has also been observed from —OH radicals [48]. This is further confirmed by the XPS analysis (presented in Fig. 4(d)), which shows that —OH radicals are formed on the NCNTP surfaces.

4.7. Effect of excitation energy on the PL of NCNTPs

Comparing Fig. 5(a) with (b), one can see that there are different PL bands generated under different excitation energies. It is known that the transition can occur when the excitation energy is larger than or equal to the energy difference between two bands. Due to the wide band-gap of small sp^2 clusters, it is difficult to excite the carriers from the conduction band to the valence band using the 532 nm excitation source. Only those clusters with small band-gaps such as large sp^2 clusters can be excited by a 532 nm laser, which results in the emission peaks at a lower energy side, which can be seen in Fig. 5(b). Moreover, when the large sp^2 clusters with lower band-gaps are excited by the 325 nm source, the high excitation energy possibly results in the generation of many phonons so that the PL efficiency is low or even quenched to produce the emission peaks at a low energy side [49].

4.8. Potential applications of NCNTPs in optoelectronic devices

Comparing the PL spectra shown in Fig. 5 with the PL results for *a*-C:H and *a*-C:N films reported by other authors [18,21], one can notice that the NCNTPs can selectively generate PL in different spectral ranges at different temperatures. For example, the blue band emission can be dramatically enhanced at low temperatures. Hence, the NCNTPs are a viable candidate material for the development of next-generation blue light emitters. According to the above analyses, the generation of a strong blue band from NCNTPs primarily originates from the band-gap increase caused by the reduction of the size of sp^2 clusters. This mechanism suggests that the blue light emitters can be fabricated by incorporating small NCNTPs into flexible organic matrices. Before the incorporation, ion bombardment can be used to increase the number of small sp^2 clusters in the NCNTPs to enhance the emission properties [50].

5. Summary

Nitrogenated carbon nanotips were synthesized from a methane, hydrogen and nitrogen reactive gas mixture using a custom-designed plasma-enhanced hot filament CVD. The morphological, structural, and photoluminescence properties of the nanostructures have been investigated by SEM, TEM, XPS, Raman spectroscopy, and PL spectroscopy. In particular, the PL results show that: (i) every spectrum consists of two emission bands centered at ~406 and ~508 nm; (ii) at low temperatures, the blue band emission becomes strongly dominant. The detailed analyses suggest that these very different emission behaviors at room and low temperatures are related to the change of the optical band-gap and the concentration of the paramagnetic defects of the carbon nanotip structures. Our results are highly-relevant to the development of the next-generation optoelectronic devices with tunable spectral responses.

Acknowledgments

This work was supported by Chongqing Natural Science Foundation of China (CSTC, 2009BA4027) and partially supported by the CSIRO's OCE Science Leadership Scheme and the Australian Research Council. Authors thank A.E. Rider for fruitful discussions and proofreading the manuscript.

REFERENCES

[1] Cao Q, Kim HS, Pimparkar N, Kulkarni JP, Wang C, Shim M, et al. Edium-scale carbon nanotube thin-film integrated circuits on flexible plastic substrates. Nature 2008;454:495–500.
[2] Ostrikov K. Colloquium: reactive plasmas as a versatile nanofabrication tool. Rev Mod Phys 2005;77:489–511.
[3] Kim TA, Kim HS, Lee SS, Park M. Single-walled carbon nanotube/silicone rubber composites for compliant electrodes. Carbon 2012;50:444–9.

[4] Cvelbar U, Chen Z, Sunakra MK, Mozetič M. Spontaneous growth of superstructure -Fe_2O_3 nanowire and nanobelt arrays in reactive oxygen plasma. Small 2008;4:1610–4.

[5] Ci L, Suhr J, Pushparaj V, Zhang X, Ajayan PM. Continuous carbon nanotube reinforced composites. Nano Lett 2008;8:2762–6.

[6] Mariotti D, Švrček V, Kim DG. Self-organized nanostructures on atmospheric microplasma exposed surfaces. Appl Phys Lett 2007;91:183111.

[7] Zhao Q, Fan T, Ding J, Zhang D, Guo Q, Kamada M. Super black and ultrathin amorphous carbon film inspired by anti-reflection architecture in butterfly wing. Carbon 2011;49:877–83.

[8] Denysenko I, Cvelbar U, Mozetič M, Azarenkov NA. Carbon nanofiber growth in plasma-enhanced chemical vapor deposition. J Appl Phys 2008;104:073301.

[9] Keidar M, Raitses Y, Knapp A, Waas AM. Current-driven ignition of single-wall carbon nanotubes. Carbon 2006;44:1022–4.

[10] Dong X, Xing G, Park MBC, Shi W, Xiao N, Wang J, et al. The formation of a carbon nanotube–graphene oxide core–shell structure and its possible applications. Carbon 2011;49:5071–8.

[11] Wang BB, Ostrikov K. Tailoring carbon nanotips in the plasma-assisted chemical vapor deposition: effect of the process parameters. J Appl Phys 2009;105:083303.

[12] Yeong KS, Boothroyd CB, Thong JTL. The growth mechanism and field-emission properties of single carbon nanotips. Nanotechnology 2006;17:3655–61.

[13] Solá F, Biaggi LA, Fonseca LF, Resto O, Lebrón CM, Meador MA. Field emission and radial distribution function studies of fractal-like amorphous carbon nanotips. Nanoscale Res Lett 2009;4:431–6.

[14] Xu L, Li S, Wu Z, Li H, Yan D, Zhang C, et al. Growth and field emission properties of nanotip arrays of amorphous carbon with embedded hexagonal diamond nanoparticles. Appl Phys A 2011;103:59–65.

[15] Liu Z, Tabakman S, Welsher K, Dai H. Carbon nanotubes in biology and medicine: *in vitro* and *in vivo* detection, imaging and drug delivery. Nano Res 2009;2:85–120.

[16] Robertson J. Recombination and photoluminescence mechanism in hydrogenated amorphous carbon. Phys Rev B 1996;53:16302–5.

[17] Chernyshov SV, Terukov EI, Vassilyev VA, Volkov AS. Radiative recombination in *a*-$Si_{1-x}C_x$:H films. J Non-Cryst Solids 1991;134:218–25.

[18] Liao M, Feng Z, Yang S, Chai C, Liu Z, Yang J, et al. Anomalous temperature dependence of photoluminescence from *a*-C:H film deposited by energetic hydrocarbon ion beam. Solid State Commun 2002;121:287–90.

[19] Ding XL, Li QS, Kong XH. Photoluminescence and bonding structure evolution of amorphous carbon films with laser intensity. Phys B 2009;404:1920–3.

[20] Iwano Y, Kittaka T, Tabuchi H, Soukawa M, Kunitsugu S, Takarabe K, et al. Study of amorphous carbon nitride films aiming at white light emitting devices. Jpn J Appl Phys 2008;47:7842–4.

[21] Papadimitriou D, Roupakas G, Dimitriadis CA, Logothetidis S. Raman scattering and photoluminescence of nitrogenated amorphous carbon films. J Appl Phys 2002;92:870–5.

[22] Ilie A, Harel O, Conway NMJ, Yagi T, Robertson J, Milne WI. Photoconductivity of nitrogen-modified hydrogenated tetrahedral amorphous carbon. J Appl Phys 2000;87:789–94.

[23] Wang BB, Cheng QJ, Chen YA, Ostrikov K. Room-temperature photoluminescence from nitrogenated carbon nanotips grown by plasma-enhanced hot filament chemical vapor deposition. J Appl Phys 2011;110:054323.

[24] Sui J, Lu JJ. Synthesis of carbon nitride powder by selective etching of $TiC_{0.3}N_{0.7}$ in chlorine-containing atmosphere at moderate temperature. Mater Chem Phys 2010;123:264–8.

[25] Kaufman JH, Metin S, Saperstein DD. Symmetry breaking in nitrogen-doped amorphous carbon: infrared observation of the Raman-active G and D bands. Phys Rev B 1989;39:13053–60.

[26] Kovács GJ, Veres M, Koós M, Radnoczi G. Raman spectroscopic study of magnetron sputtered carbon–nickel and carbon nitride–nickel composite films: The effect of nickel on the atomic structure of the C/CN_x matrix. Thin Sol Films 2008;516:7910–5.

[27] Wang BB, Zhang B. Effects of carbon film roughness on growth of carbon nanotip arrays by plasma-enhanced hot filament chemical vapor deposition. Carbon 2006;44:1949–53.

[28] Filik J, May PW, Pearce SRJ, Wild RK, Hallam KR. XPS and laser Raman analysis of hydrogenated amorphous carbon films. Diam Relat Mater 2003;12:974–8.

[29] Zheng WT, Cao PJ, Li JJ, Wang X, Jin ZS. Chemical bonding of CN_x films synthesized by nitrogen ion implantation into diamond and graphite. Surf Coat Technol 2003;173:213–8.

[30] Gardner SD, He G, Pittman CU. A Spectroscopic examination of carbon fiber cross sections using XPS and ISS. Carbon 1996;34:1221–8.

[31] Wang BB, Zhu MK, Hu N, Li LJ. Raman scattering and photoluminescence of zinc telluride nanopowders at room temperature. J Lumin 2011;131:2550–4.

[32] Hu J, Yang P, Lieber CM. Nitrogen-driven sp^3 to sp^2 transformation in carbon nitride materials. Phys Rev B 1998;57:R3185–8.

[33] Wang BB, Cheng QJ, Zhong XX, Wang YQ, Chen YA, Ostrikov K. Enhanced electron field emission from plasma-nitrogenated carbon nanotips. J Appl Phys 2012;111:044317.

[34] Nagai H, Takashima S, Hiramatsu M, Hori M, Goto T. Behavior of atomic radicals and their effects on organic low dielectric constant film etching in high density N_2/H_2 and N_2/NH_3 plasmas. J Appl Phys 2002;91:2615–21.

[35] Mandal SK, Samanta S, Itkis ME, Jensen DW, Reed RW, Oakley RT, et al. Resonating valence bond ground state in oxygen-functionalized phenalenyl-based neutral radical molecular conductors. J Am Chem Soc 2006;128:1982–94.

[36] Sun CQ, Tay BK, Lau SP, Sun XW, Zeng XT, Li S, et al. Band contraction and lone pair interaction at nitride surfaces. J Appl Phys 2001;90:2615–7.

[37] Sun CQ. Size dependence of nanostructures: impact of bond order deficiency. Prog Solid State Chem 2007;35:1–159.

[38] Varshni YP. Temperature dependence of the energy gap in semiconductors. Physica 1967;34:149–54.

[39] Watanabe I, Okumura T. Photo-induced ESR in amorphous C:H films prepared by glow discharge decomposition of CH_4 and H_2. Jpn J Appl Phys 1985;24:L122–4.

[40] Zhang M, Nakayama Y. Effect of ultraviolet light irradiation on amorphous carbon nitride films. J Appl Phys 1997;82:4912–5.

[41] Fanchini G, Tagliaferro A, Conway NMJ, Godet C. Role of lone-pair interactions and local disorder in determining the interdependency of optical constants of a-CN:H thin films. Phys Rev B 2002;66:195415.

[42] Souto S, Pickholz M, Santos MCD, Alvarez F. Electronic structure of nitrogen-carbon alloys (*a*-CN_x) determined by photoelectron spectroscopy. Phys Rev B 1998;57:2536–40.

[43] Füle M, Budai J, Tóth S, Veres M, Koós M. Size of spatial confinement at luminescence centers determined from resonant excitation bands of *a*-C:H photoluminescence. J Non-Cryst Solids 2006;352:1340–3.

[44] Heitz T, Godet C, Bourée JE, Drévillon B, Conde JP. Radiative and nonradiative recombination in polymerlike α-C:H films. Phys Rev B 1999;60:6045–52.
[45] Godet C, Heitz T, Bourée JE, Drévillon B, Clerc C. Growth and composition of dual-plasma polymer-like amorphous carbon films. J Appl Phys 1998;84:3919–32.
[46] Casiraghi C, Ferrari AC, Robertson J. Raman spectroscopy of hydrogenated amorphous carbons. Phys Rev B 2005;72:085401.
[47] Capozzi V, Trovato T, Berger H, Lorusso GF. Photoluminescence spectra of C_{60} thin films deposited on different substrates. Carbon 1997;35:763–6.
[48] Ray SC, Fanchini G, Tagliaferro A. Luminescence, recombination and laser damaging of *a*-CN:OH films grown by reactive sputtering. J Mater Sci 2005;40:5451–5.
[49] Rusli R, Robertson J, Amaratunga GAJ. Photoluminescence behavior of hydrogenated amorphous carbon. J Appl Phys 1996;80:29983003.
[50] Wang BB, Wang WL, Liao KJ, Xiao JL. Experimental and theoretical studies of diamond nucleation on silicon by biased hot filament chemical vapor deposition. Phys Rev B 2001;63:085412.